Electronic Supplementary Material (ESI) for RSC Advances.
This journal is © The Royal Society of Chemistry 2020

Electronic Supplementary Information (ESI) for

# Impact of oxygen defects on ferromagnetic $CrI_3$ monolayer

Batjargal Sainbileg, ‡[ab] Erdembayalag Batsaikhan ‡[ab] and Michitoshi Hayashi*[ab]

[a]Center for Condensed Matter Sciences, National Taiwan University, Taipei 106, Taiwan.

[b]Center of Atomic Initiative for New Materials, National Taiwan University, Taipei 106, Taiwan.

‡ These authors contributed equally.

*Corresponding author e-mail: atmyh@ntu.edu.tw

**Table of Contents**

**Scheme S1**. Illustration of calculations for binding energy per oxygen.

**Scheme S2.** Illustration of calculations for formation energy of O-defective $CrI_3$ monolayers.

**Fig. S1**. Ab initio Molecular dynamical (AIMD) calculations of O-defective $CrI_3$ monolayers.

**Fig. S2.** Possible magnetic configurations of $CrI_3$ monolayer.

**Fig. S3.** Schematic illustration of Cr orbitals and the corresponding magnetic exchanges.

**Fig. S4**. Band-gap reduction in the minority spin channel of band structure.

**Fig. S5**. Band-decomposed partial charge density of all investigated $CrI_3$ monolayers.

**Fig. S6**. 3D and 2D contour plots of the charge density for O-attached $CrI_3$.

**Fig. S7**. 3D and 2D contour plots of the charge density for O-doped $CrI_3$.

**Fig. S8**. Electron localization function (ELF) profile of all investigated $CrI_3$ monolayers.

**Table. S1** Bond Length and the bond angle between other Cr- I (O) around the reference unit.

**Reference**

**Details of binding and formation energies**

In the main text, we have used the spin-polarized PBE functional including both plus +U method and van der Waals D3 corrections (PBE+U-D3), in order to predict 3d states accurately and obtain a reliable structure for investigating the magnetic and electronic properties of the present $CrI_3$ monolayers. The binding energy per oxygen atom and formation energies of defective monolayers are also estimated in terms of PBE+U-D3 accordingly and our results are consistent with the trend of TMDs with single atomic defects. [S1-S2] In particular, Dobrota et al[S1] have shown that the binding energy of a non-metallic single dopant on the graphene is large, ranging from -7.3 eV to -15.5 eV. Moreover, Dabral et al[S2] have reported that an oxygen atomic defect on common 2D TMDs has large binding energy (-7.5 eV to -11 eV) whose values of a single-oxygen-atomic defect are much larger than the binding energy of $H_2O$ and $O_2$ molecules on those 2D TMDs.

In this ESI, in order to compare with the early literature devoting to some well-known 2D materials, we also have calculated of binding per oxygen atom and formation energies of present $CrI_3$ monolayers, with similar computational conditions in the literature[S3-S4], without the plus +U functional and vdW D3 corrections. As a result, we found that binding energy per oxygen atom and formation energies on defective $CrI_3$ are obviously different with and without the plus +U functional and vdW D3 corrections. The simulated values with different methods are given in Scheme 1 and Scheme 2, together with the calculation steps. Our finding is consistent with a trend in the previous literature that the binding and formation energies strongly depend on the selected functional. [S5-S6]

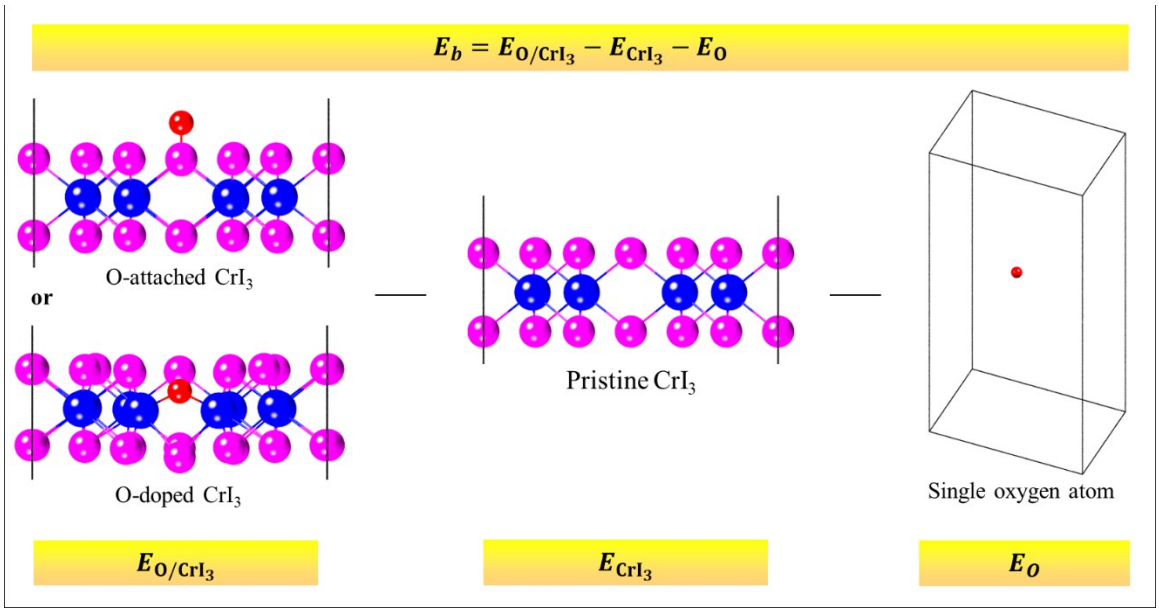


**Scheme S1.** Illustration of calculations for the binding energy per an oxygen atom on defective $CrI_3$ monolayers. Note that binding energies are -9.4 eV (PBE+U-D3) and -0.14 eV (PBE) for O-attached $CrI_3$ while binding energies are -9.6 eV (PBE+U-D3) and -1.76 eV (PBE) for O-doped $CrI_3$.

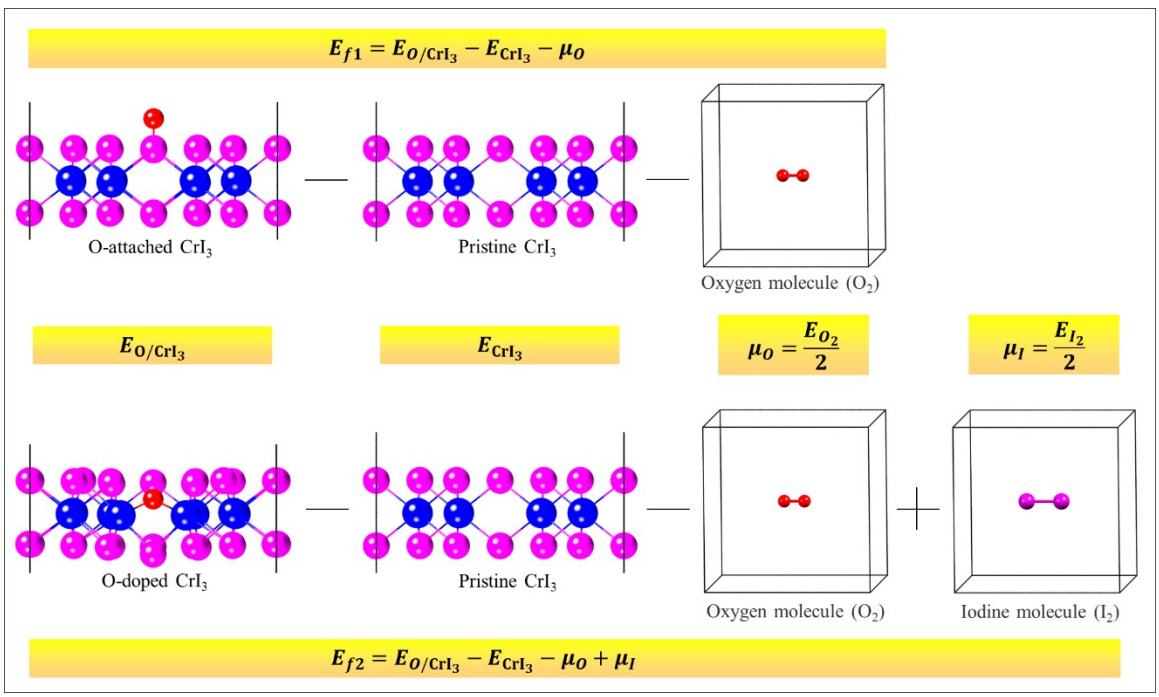


**Scheme S2.** Illustration of calculations for the formation energy of defective $CrI_3$ monolayers. Formation energies are -6.4 eV (PBE+U-D3) and -0.14 eV (PBE) for O-attached $CrI_3$ while formation energies are -7.9 eV (PBE+U-D3) and -1.69 eV (PBE) for O-doped $CrI_3$.

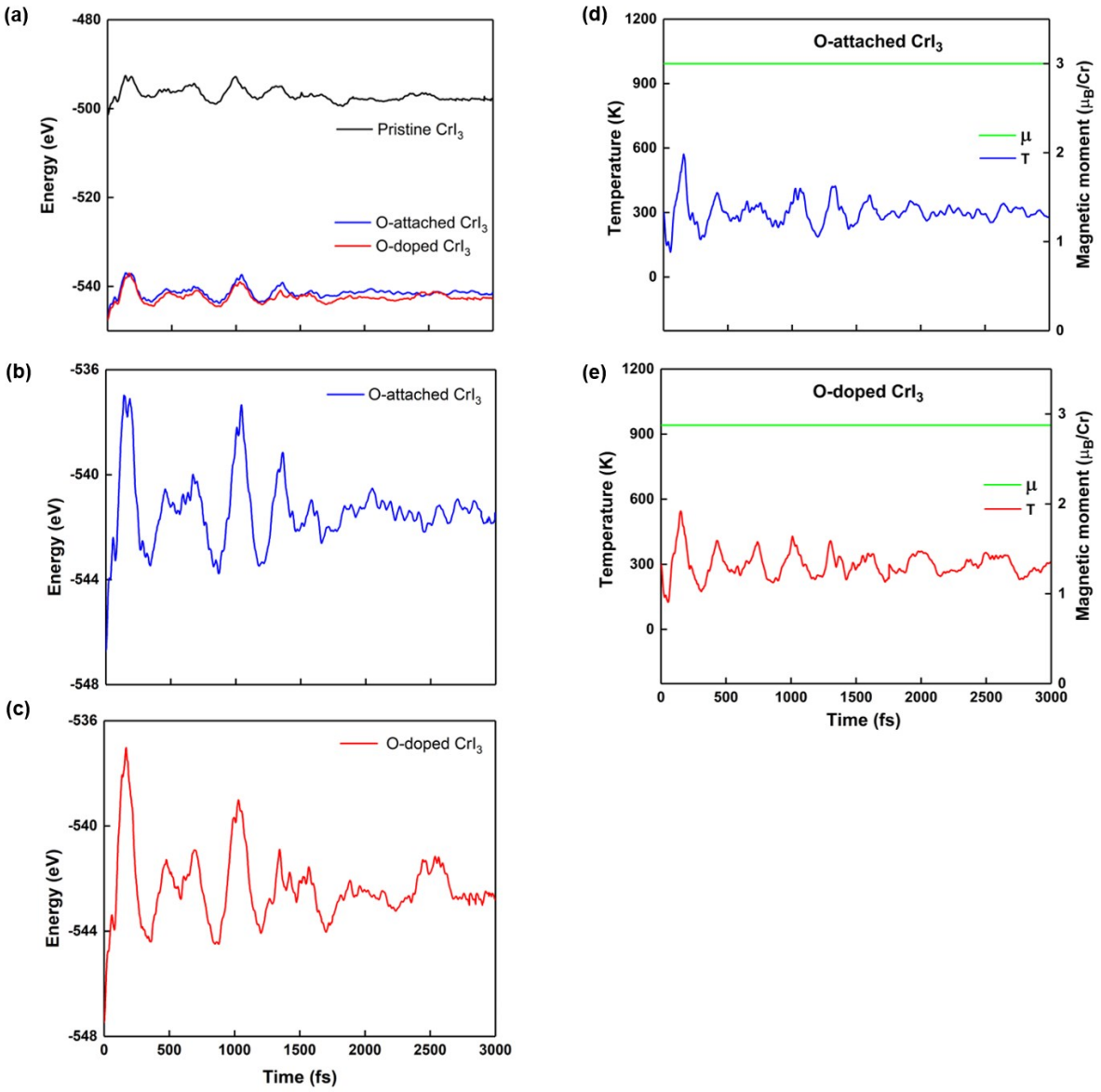


**Fig. S1.** (a) Calculated AIMD evolutions of energy for O-attached (blue) and O-doped (red) $CrI_3$ monolayers comparing with pristine $CrI_3$ (black), being thermally more favorable than pristine $CrI_3$ monolayer. The enlarged graphs with an adequate scale of the vertical axis of (b) O-attached and (c) O-doped $CrI_3$ monolayer are plotted, respectively. (d-e) Temperature (right Y-axis) and magnetic moment (left Y-axis) for the defective monolayers. Remarkably, the time-evolutions of the magnetic moment maintain constant during AIMD simulations (see green line in Fig. S1d and Fig.S1e).

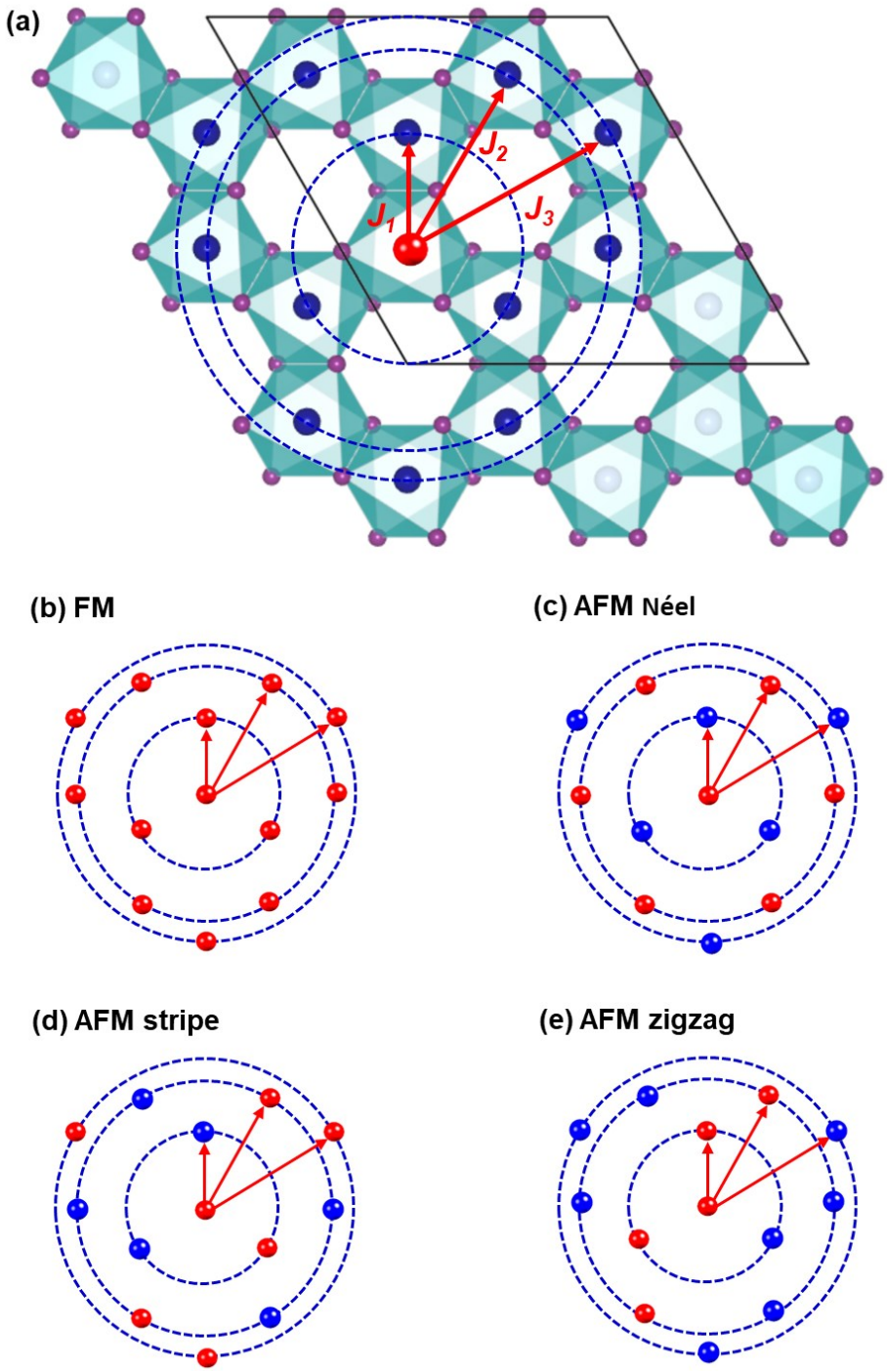


**Fig. S2.** (a) Schematic view of possible exchange interaction paths between Cr ions in $CrI_3$ monolayer; $J_1$, $J_2$, and $J_3$ represent exchange interactions in the 1st-, 2nd-, and 3th- nearest-neighbors (NN) while the dashed circles illustrate the horizon of each path. (b-e) The possible magnetic configurations of $CrI_3$ monolayer. The red (blue) ball depicts the spin-up (spin-down).

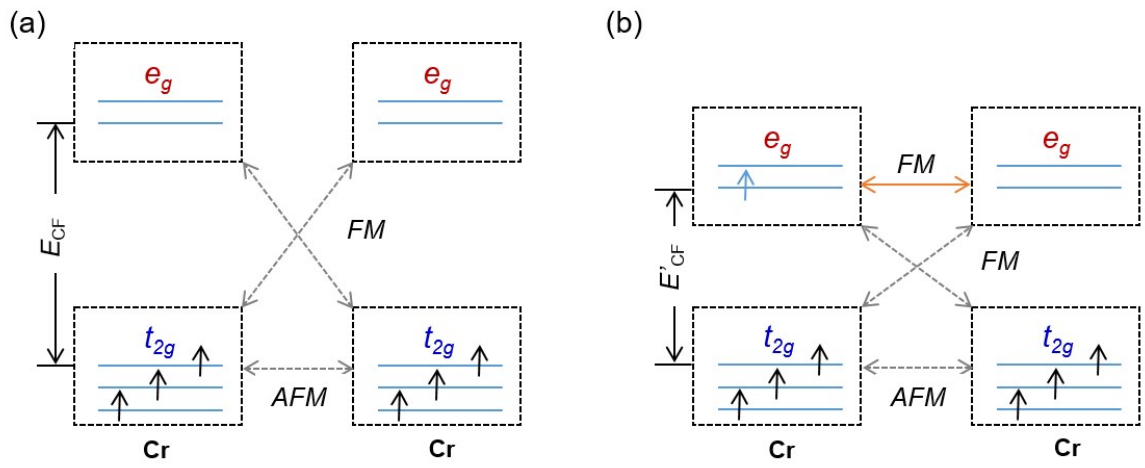


**Fig. S3.** Schematic illustration[S7] of Cr orbitals and the corresponding magnetic exchanges in (a) pristine $CrI_3$ and (b) O-doped $CrI_3$. Herein, $E_{CF}$, $E'_{CF}$, FM, and AFM stand for the crystal-field, reduced crystal-field, ferromagnetic exchange, and antiferromagnetic exchange while the dashed and solid arrow lines represent possible virtual and real hopping, respectively.

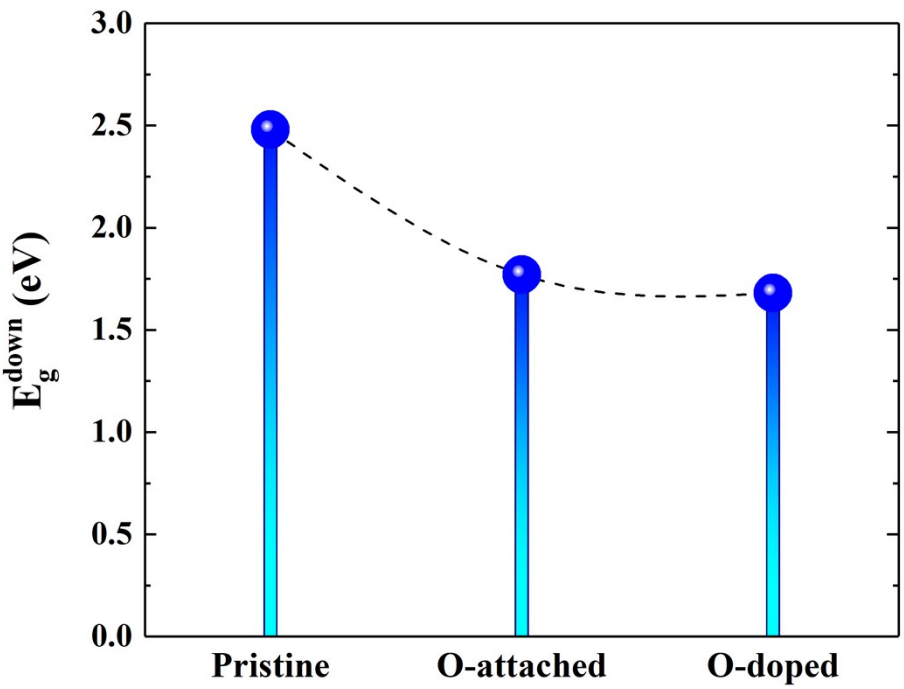


**Fig. S4.** Band-gap reduction in the minority (↓) spin channel of band structure for defective $CrI_3$ with respect to that of pristine monolayer.

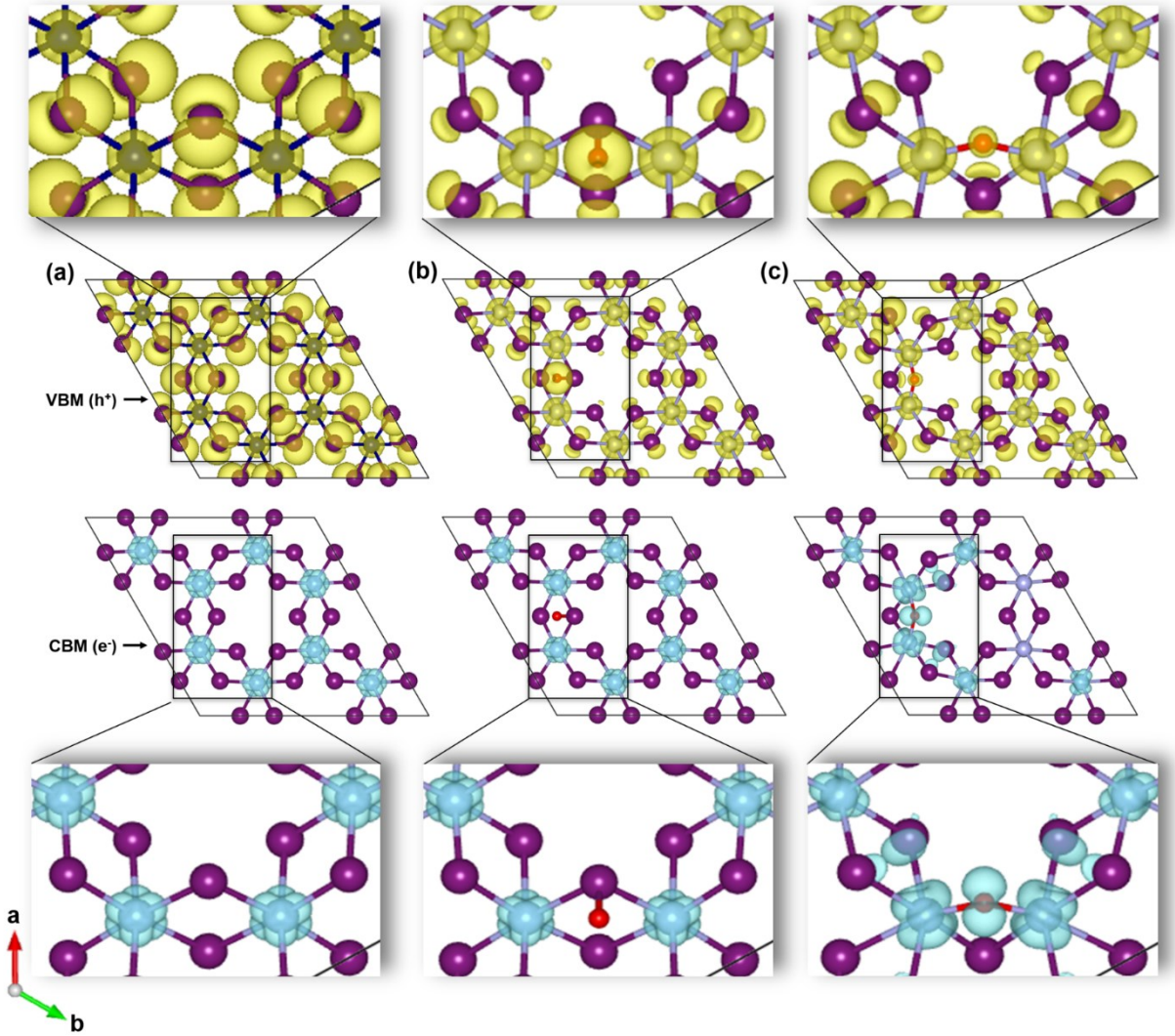


**Fig. S5.** Isosurfaces for the band-decomposed partial charge density of VBM (top panel) and CBM (bottom panel) of (a) pristine, (b) O-attached, and (c) O-doped $CrI_3$ monolayer, respectively, where the cyan (yellow) isosurfaces represent the distribution of electrons (holes) charge density at the CBM (VBM). The black box depicts the zoomed-in view of the unit selected from the monolayer.

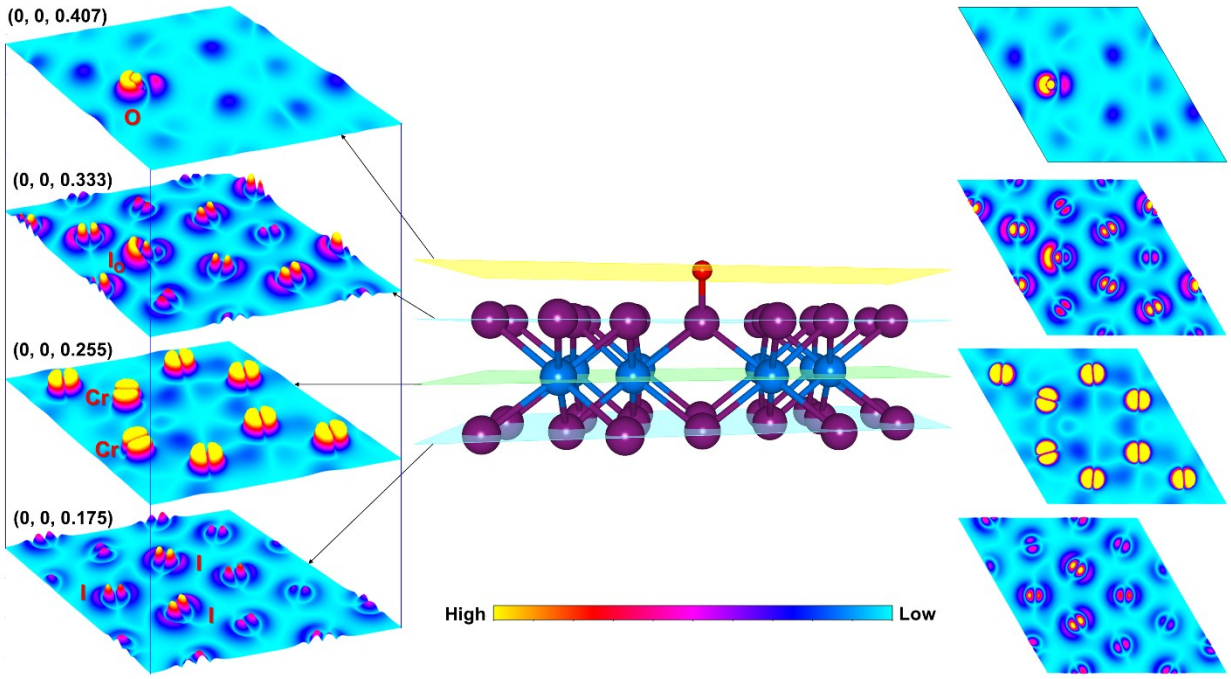


**Fig. S6.** 3D (left panel) and 2D (right panel) contour plots of the charge density for O-attached $CrI_3$ along the (001) crystallographic directions at z = 0.175, 0.255, 0.333, and 0.407.

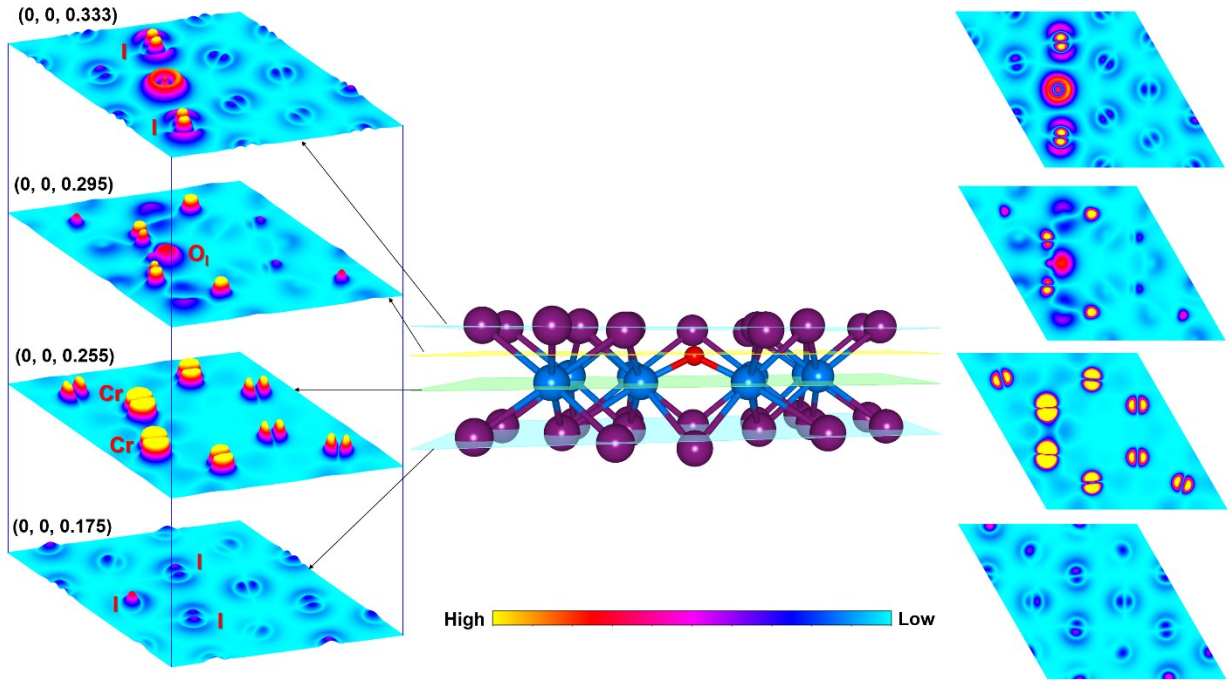


**Fig. S7.** 3D (left panel) and 2D (right panel) contour plots of the charge density for O-doped $CrI_3$ along the (001) crystallographic directions at z = 0.175, 0.255, 0.295, and 0.333.

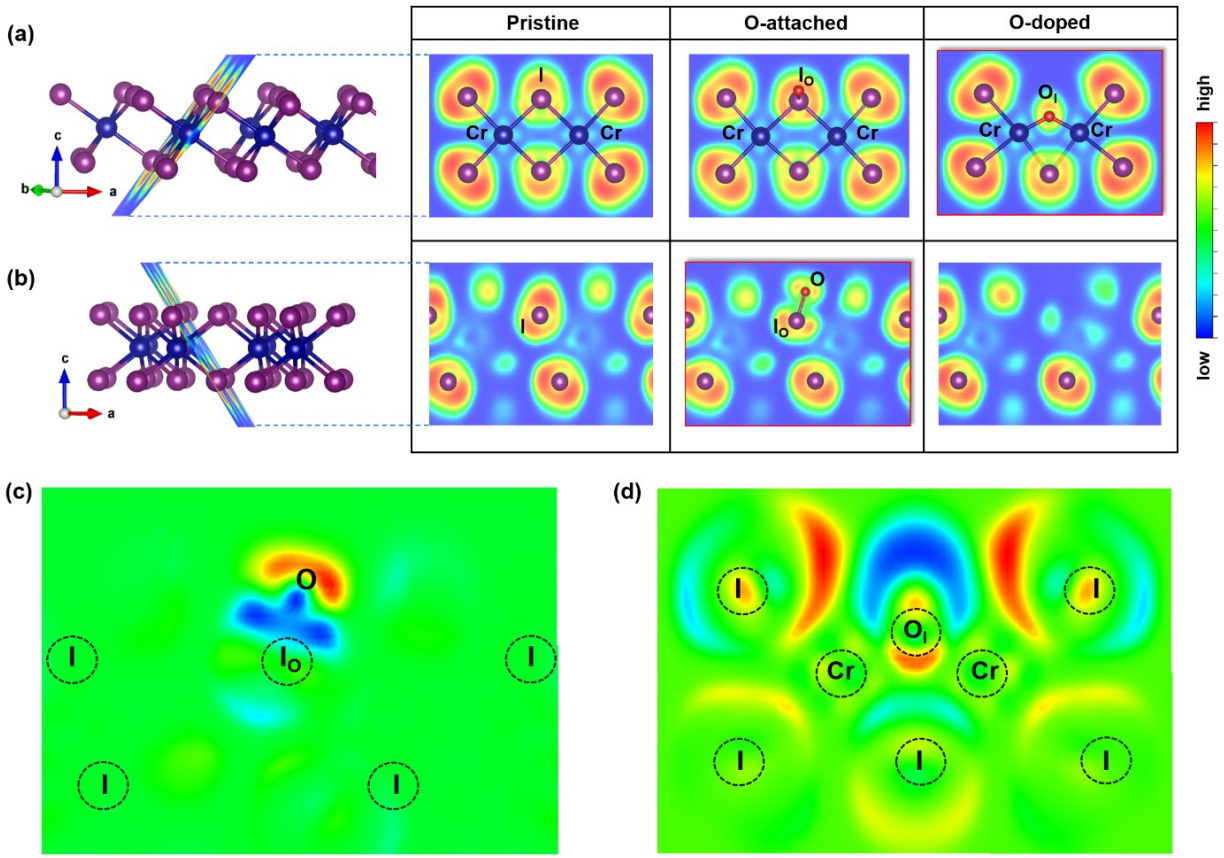


**Fig. S8.** The electron localization function (ELF) profile provides the change of charge density distribution. ELF maps of all investigated $CrI_3$ monolayers are along (a) [-2 1 2] and (b) [1 0 1] crystallographic planes. This result reveals that the ELF map along [-2 1 2] plane is nearly identical in both the pristine and O-attached monolayer whereas the ELF map is different in the O-doped monolayer. Moreover, (c-d) illustrate the ELF difference ($\Delta^{ELF}$) of O-attached monolayer along [-2 1 2] plane and O-doped along [1 0 1] plane, where the dashed-circle represents the preferred location of atoms at the selected slice. Notably, **Fig. S8c** displays that the $I_O$-atom lost the noticeable amount of charges to the O-atom while the ELF on the rest of Cr- and I-atoms remain unchanged in O-attached monolayer, indicating that the O-dangling locally affects its neighboring $I_O$-atom, but less the $CrI_3$ monolayer. Meanwhile, **Fig. S8d** shows that there is weak but obvious charge accumulation between Cr-$O_I$-Cr atoms in O-doped monolayer.

**Table. S1** Length (L) and the corresponding angle (∠) between other Cr- I (O) bonds surrounding the reference unit discussed in the manuscript.

| | Configuration | Pristine $CrI_3$ | O-attached $CrI_3$ | O-doped $CrI_3$ |
|---|---|---|---|---|
| Geometry | | 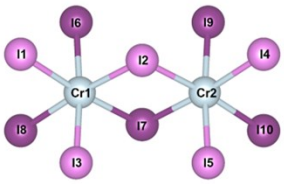 | 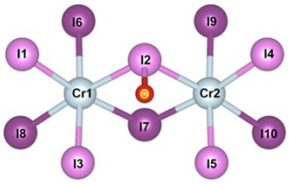 | 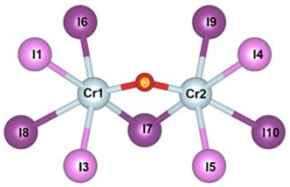 |
| Bond angle (°) | $\angle(I_1\text{-}Cr_1\text{-}I_2/O)$ | 90.03 | 89.72 | 103.22 |
| | $\angle(I_2/O\text{-}Cr_1\text{-}I_3)$ | 90.03 | 89.44 | 92.9 |
| | $\angle(I_3\text{-}Cr_1\text{-}I_1)$ | 90.03 | 89.46 | 85.29 |
| | $\angle(I_1\text{-}Cr_1\text{-}I_8)$ | 93.39 | 94.84 | 88.02 |
| | $\angle(I_2/O\text{-}Cr_1\text{-}I_6)$ | 93.39 | 91.02 | 102.37 |
| | $\angle(I_1\text{-}Cr_1\text{-}I_7)$ | 175.29 | 175.28 | 166.17 |
| | $\angle(I_2/O\text{-}Cr_1\text{-}I_8)$ | 175.29 | 174.11 | 173.23 |
| | $\angle(I_8\text{-}Cr_1\text{-}I_7)$ | 90.01 | 91.33 | 86.68 |
| | $\angle(I_6\text{-}Cr_1\text{-}I_7)$ | 90.01 | 90.55 | 92.91 |
| | $\angle(I_6\text{-}Cr_1\text{-}I_8)$ | 90.01 | 92.29 | 86.88 |
| Bond length (Å) | $L(Cr_1\text{-}I_1)$ | 2.74 | 2.74 | 2.78 |
| | $L(Cr_1\text{-}I_3)$ | 2.74 | 2.73 | 2.76 |
| | $L(Cr_1\text{-}I_6)$ | 2.74 | 2.73 | 2.72 |
| | $L(Cr_1\text{-}I_8)$ | 2.74 | 2.74 | 2.94 |

**References:**


[S1]. A.S. Dobrota, I.A. Pašti, S. V. Mentus, and N.V. Skorondumova. *Phys.Chem.Chem.Phys*., 2017, **19**, 8530.

[S2]. A. Dabral, A. K. A. Lu, D. Chiappe, M.Houssa, and G. Pourtois, *Phys.Chem.Chem.Phys*., 2019, **21**, 1089.

[S3]. G. Wang, R. Pandey, and S.P. Karna. *Nanoscale*, 2015, **7**, 524.

[S4]. S. KC, R. C. Longo, R. M. Wallace, and K. Cho. *J. Appl. Phys*., 2015, **117**, 135301.

[S5]. L. Wang, T. Maxisch, and G. Ceder. *Phys. Rev. B*., 2006, **73**, 195107.

[S6]. A. Jain, G. Hautier, S. P. Ong, C. J. Moore, C. C. Fischer, K. A. Persson, and G. Ceder. *Phys. Rev. B*., 2011, **84**, 045115.

[S7]. Y. Zhao, L. Lin, Q. Zhou, Y. Li, S. Yuan, Q. Chen, S. Dong, and J. Wang. *Nano Lett*., 2018, **18**, 2943–2949.